Leaching behaviour of Cs, Sr, and Eu nitrates from Fe-rich polymers: Influence of precursor composition, presence of CeO_2 nanoparticles, and the effect of high-dose gamma irradiation

E. D. Mooren[1,2*], S. Van Winckel[2], R. Alvarez- Sarandes[2], A. Cambriani[2], L. Fongaro[2], W. Bonani[2], G. Beersaerts[3], V. Tyrpekl[4], T. Cernousek[5], S. Schreurs[1], R. J. M. Konings[2,6], W. Schroeyers[1]

[1]*Hasselt University, CMK, Nuclear Technological Centre (NuTeC), Faculty of Engineering Technology, Agoralaan, Gebouw H, 3590 Diepenbeek, Belgium*
[2]*European Commission, Joint Research Centre (JRC), Germany*
[3]*KU Leuven, Department of Materials Engineering, Kasteelpark Arenberg 44, 3001 Leuven, Belgium*
[4]*Department of Inorganic Chemistry, Faculty of Science, Charles University, Hlavova 2030/8, 128 43, Prague, Czech Republic*
[5]*Department of Material Analysis, Research Centre Rež Ltd., Hlavn ˇ í 130, 250 68 Husinec, Czech Republic*
[6]*Faculty of Applied Sciences, Radiation Science & Technology Department, Delft University of Technology, Mekelweg 15, Delft 2629JB, the Netherlands*

Abstract

The extended half-lives and potential for environmental contamination of radionuclides in liquid nuclear waste make radioactive waste management a major concern for society and the nuclear industry. One prospective solution for efficiently managing liquid nuclear waste is the use of Alkali-Activated Materials (AAMs). The immobilisation ability of AAMs largely depends on their composition and the effect of the introduced radionuclides on the structure itself. The purpose of this work is to investigate the leaching behaviour of radioactive simulants such as strontium (Sr), caesium (Cs), and europium (Eu) nitrates from iron-rich slag-derived AAM samples, explore the impact of CeO_2 nanoparticles` presence as well as the effects of gamma irradiation on the structure and leachability of the contaminants. CeO_2 nanoparticles are investigated for preconcentrating radionuclides from liquid nuclear waste and have been previously used in isolating and absorbing Eu^{3+}. Samples received a cumulative dose of 6.5 MGy of radiation from a cobalt-60 (^{60}Co) source. Potential changes in mechanical characteristics and microstructure were investigated by SEM analysis and nanoindentation. The leaching tests revealed significant variability in the release of elements such as Fe, Na, Al, Cs, Sr, Eu, and Ce across different samples, influenced by the slag composition and the presence of CeO_2 nanoparticles. No appreciable variations were observed in the dopant or structural element releases from the irradiated and non-irradiated samples. Irradiation had no effect on the materials' hardness and a limited effect on elastic modulus. From this perspective, the produced AAMs are suitable candidates for nuclear waste immobilisation.

Keywords

Alkali Activated Materials, Geopolymers, Dynamic Leaching, Nanoparticles, Immobilization, Radioactive Waste, Gamma Irradiation

1. Introduction

Safe handling and disposal of radioactive waste (RAW) has gained more attention as nuclear power and the corresponding nuclear fuel cycles have developed [1], [2]. Continuous production of electricity from nuclear power is responsible for significant quantities of spent fuel, which has a long-term radiotoxicity. In addition to the mostly -relatively speaking- short-lived fission products like $^{134+137}Cs$ and ^{90}Sr, the spent fuel also contains a sizable amount of the higher actinides with much longer half-lives [3]. Effective immobilization of radioactive actinides and lanthanides in groundwater, wastewater, soil, etc., is a key objective in the treatment of radioactive waste. As a chemical analogue

of trivalent lanthanides and actinides (e.g. Am(III)), europium is typically selected for studying nuclear waste treatment and immobilisation [4], [5].

Researchers have been looking into the development of more efficient alternatives of Ordinary Portland Cement (OPC) for the immobilisation and long-term storage of nuclear waste stream forms. The alternatives include matrices of the alkali activated materials (AAMs) type, inorganic polymers (based on metakaolin and sodium silicate), calcium-aluminate cement, and calcium-sulfoaluminate cement [2]. AAMs have shown to have better mechanical properties compared to OPC concretes, improved long-term properties including tensile strength, creep coefficient, and modulus of rupture, in addition to low permeability, long-term durability, high-temperature resistance (up to 1200 °C), and remarkable fire and acid resistance [6]–[9]. AAMs (or subclasses thereof) are referred to by a number of different names, including geopolymers, inorganic polymers, soil cements, geocements, alkaline cements, zeoceramics, alkali-activated slag cement, and others, depending on the kind of precursor and the chemical composition of the hydration products [10], [11]. These materials have drawn a lot of interest due to their possible use in the immobilisation of radioactive waste [12]–[14]. They are a viable substitute for conventional ordinary Portland cement (OPC)-based matrices because they have favourable qualities such as high early strength, moderate shrinkage, and outstanding resistance to chemical attack [15]. Previous studies indicate that AAMs have proven to have exceptional mechanical and thermal qualities, including compressive strengths of more than 100 MPa. Furthermore, research has demonstrated that geopolymers can endure temperatures as high as 500°C without losing any of their residual strength [16].

The capability of alkali-activated materials to effectively immobilize and confine radionuclides such as caesium and strontium is a crucial feature for radioactive waste encapsulation. It is critical to comprehend how these elements leak from waste encapsulation forms based on AAMs and how radiation affects the characteristics of the AAM matrix [17]. AAMs have shown encouraging results in the immobilisation of radionuclides including ^{90}Sr and $^{134+137}Cs$ [18]–[21]. Apart from successfully immobilising Cs^{+} and Sr^{2+}, AAMs have also effectively immobilised mobile ions including Cd^{2+} and Pb^{2+} [22], as well as radionuclides like ^{152}Eu, ^{60}Co, ^{59}Fe, and isotopes of Am and Pu in different ionic forms [23]–[25]. Multiple studies have been carried out on the immobilisation of Cs and Sr in AAMs [12], [14], [26]–[28], leaving the immobilisation of Eu in AAMs less investigated.

One method of isolating and absorbing Eu^{3+} is the use of CeO_2 nanoparticles. CeO_2 nanoparticles were proven to be effective absorbents for Eu^{3+}, Gd^{3+}, and Yb^{3+} in aqueous solutions [29]. CeO_2 nanoparticles are considered as a preconcentration step to isolate radionuclides from RAW before the final immobilisation via cementitious binders. These nanoparticles will also eventually need to be disposed of after being used in multiple adsorption/desorption cycles. While the majority of the research on the use of AAMs for RAW immobilization discusses AAMs based on commercial recipes, metakaolin (MK), fly ash (FA), ground granulated blast furnace slag (GGBFS), or mixtures of these [13], [14], [28], [30], iron-silicate based AAMs have been investigated to a lesser extent. Iron-silicate based AAMs include non-ferrous metallurgy slags like Cu, Pb, and FeNi slags as well as ferrous metallurgy slags like electric arc furnace steel slags and blast furnace slags [31]. Furthermore, there are not enough high-value applications yet for fayalite slags from the nonferrous metal sector [32], especially as an approach to immobilise radionuclides.

When considering the application of alkali-activated materials for nuclear waste immobilization, it is important to determine the relevant doses of gamma irradiation that these materials can withstand [33]. Tests have been conducted on cementitious binders to demonstrate their stability under

radiation and their capacity to serve as radiation shields [2]. Research has been done on the effects of radiation on the mechanical, structural, and physicochemical characteristics of AAMs. Mast et al. [34] studied the impact of high dose rate gamma irradiation on mechanical and microstructural properties and on the curing process of $CaO\text{-}Fe_xO_y\text{-}SiO_2$ slag-based inorganic polymers. Samples that were hardened for longer times appeared to be less affected by the gamma irradiation. The response to irradiation was highly dependent on the initial condition of the samples. Overall, irradiation led to increased compressive strength, decreased Young's modulus and creep, and changes in the Fe^{3+}/Fe^{2+} ratio in the less hardened samples. Ionizing radiation can also cause reactive intermediates and free radicals to develop in polymers, which can alter the material's migration limits and barrier qualities [35]. Yeoh et al. [36] investigated the effects of long-term gamma irradiation on the mineralogical, microstructural, structural, physical, and chemical properties of AAM pastes based on blast furnace slags (BFS) and fly ash (FA) slags. They found that irradiation for 2 months (1574 kGy) increases the compressive strength by ~45% through the conversion of less-crosslinked to more-crosslinked silicate species. Furthermore, beneficial primary effects of gamma irradiation on compressive strength were observed at low dosages (95 kGy) with adequate curing time (28 days). They also observed that gamma irradiation has little impact on the aqueous leaching of AAM pastes. This suggests that these materials could be used as efficient storage solutions for intermediate-level waste forms, able to surpass the efficiency of products based on Portland cement [36]. Deng et al. [17] discovered that gamma irradiation with a cumulative dosage of 100 KGy, caused a few alterations in FA-based AAM matrices. The Si–Al tetrahedral coordination connected by oxygen bridges remained stable under all leachants following irradiation, according to Si and Al mapping studies. However according to a Mercury Intrusion Porosimetry (MIP) study, irradiation considerably altered the pore size distributions in the waste forms, and the irradiated samples' porosity (12.9%) rose in comparison to the non-irradiated samples (11.6%) [17]. Mahrous et al. [37] found that the mechanical strength of the metakaolin-based AAMs was significantly increased despite the increase in surface cracking caused by ion irradiation, mimicking neutron irradiation. Measurements using nanoindentation showed a stunning 90% increase in microhardness, a 46% increase in reduced modulus (E_r), and a 23% decrease in contact depth, all of which are signs of improved stiffness and resistance to deformation [37]. Consequently, the behaviour of AAM matrices subjected to gamma irradiation greatly depends on their composition and irradiation dosage.

The effects of much higher radiation doses, such as the one employed in this study, on the physicochemical, structural, and mechanical properties of iron-rich AAM matrices, and their leachability after irradiation, remain largely unexplored. This study is combining the use of inorganic polymers as well as sorption by nanoparticles in order to develop a long-term storage solution for radionuclides found in nuclear waste. Furthermore, the retention capacity of three distinct AAM matrices is examined after high dose of gamma irradiation. The materials were doped with non-radiological chemical analogues $CsNO_3$, $Sr(NO_3)_2$, and $Eu(NO_3)_3$, to simulate the radionuclides $^{134+137}Cs$, ^{90}Sr, and $^{152+154}Eu$, in order to assess their retention in the AAM matrix and the effect of the presence of CeO_2 nanoparticles as well as the impact of high-dose gamma irradiation exposure. Up-flow percolation experiments, a dynamic form of leaching, were performed on the samples, and Inductively Coupled Plasma Mass Spectrometry (ICP-MS) was used to evaluate the outcomes.

Van der Sloot et al. [38], [39] propose an alternative leaching assessment approach for cementitious materials used for immobilization of radionuclides and other radionuclide containing wastes that is related to specific management scenarios rather than the total content. The aim of this alternative leaching assessment is to provide, for waterborne pathways, a more robust health and environmental risk assessment. A set of leaching tests (a.o. pH dependence test, percolation leaching test and mass

transfer test) are proposed to consider the release pathways for example linked to the disposal and in this way study the most important factors that determine the potential environmental impact. For example, an aspect that is sometimes neglected during environmental assessments is the water exchange that results from a combination of capillary uptake, vapor migration and condensation as was documented for the low-level nuclear waste vaults in Spain [40]. When the damage level to the matrix increases, water exchange by percolation increases owing to increased hydraulic conductivity when the surrounding environment contains a sufficient amount of water. To contribute to a more robust health and environmental risk assessment, the up-flow percolation test in accordance with the CEN/TS 16637-3 standard [41] is used in our research approach. Samples were leached without being subjected to irradiation and after irradiating. Additional investigations using nanoindentation and image analysis were performed in order to evaluate the structural properties and microstructure of irradiated and non-irradiated materials. The results of this investigation can be utilised to enhance the blueprint of an immobilisation matrix based on ferrosilicates and assess the influence of gamma irradiation on the retention capacity as well as the structural properties of the matrices.

2. Experimental methods

2.1. *AAM synthesis*

Three slags were synthesised by the Sustainable Resources for Engineered Materials (SREM) team at the KU Leuven Department of Material Engineering as described by Pontikes et al. [42]. The quenched slags were ground into a powder using an attritor (1S Wiener) to produce a specific surface area of roughly 3800 g/cm². Table 1 shows the composition of the slags as determined by X-Ray Fluorescence (XRF) using a Brucker axs S8 Tiger spectrometer. Before the XRF measurement, the slags were dried at 100°C overnight. All three slags have SrO, according to the XRF analysis, even though the amount was only trace amounts and below the instrument's sensitivity threshold and quantification limit. An activator consisting of a sodium silicate solution with molar ratios of 1.6 for SiO_2/Na_2O and 25 for H_2O/Na_2O was employed. A commercial silicate solution (molar ratio SiO_2/Na_2O = 3.48, 65 weight % H_2O, Supelco, Merck), pure NaOH pellets (Sodium hydroxide, Pellets, Pure, Bernd Kraft GmbH), and demineralized water were combined to create this solution. Non-radioactive caesium nitrate (1 wt% $CsNO_3$, Alfa Aesar 99.8%), strontium nitrate (0.1 wt% $Sr(NO_3)_2$, Supelco), and europium nitrate (1 wt% $Eu(NO_3)_3$, Thermo Scientific Chemicals 99.9%) were added to various AAM compositions to simulate the radionuclides $^{134+137}Cs$, ^{90}Sr, and $^{152+154}Eu$. A modified method of adding the activation solution to the slag was used. Water required to maintain the H_2O/Na_2O ratio at 25 was first added to the slag, followed by the remaining sodium silicate solution. This ensured even dispersion of the dopants, maximising sample homogeneity, as the dopants were initially dissolved or dispersed in the water. The slag containing the dissolved dopants and the remaining sodium silicate activating solution were combined for 60 seconds using a mechanical stirrer and then put into moulds measuring 25 x 25 x 25 mm³. The mortars were covered to prevent them from drying out, and after 24 hours, they were removed from the moulds. After that, the samples were cured for at least 28 days at room temperature. The mass ratio of the slag to solution in each sample was 0.39. Table 2 presents the various matrix designs. The samples are labelled "AAM", which is followed by a number 1 , 2 or 3 reflecting the dopant combination (Table 2) and either S1, S2, or S3 depending on which slag was used to make them (Table 1). Samples with “IRR” at the end of the name were irradiated.

Table 1. XRF analysis of the precursor slags' chemical composition in weight per cent (wt%), including the molar ratios of iron and calcium oxide to silica, and iron oxide to calcium oxide. For values over 20 wt% estimated error is 20 %, values 1-20 wt% at 50%, below 1 wt% estimated error 80%.

	wt% Fe_xO_y	*wt% SiO_2*	*wt% CaO*	*wt% Al_2O_3*	*wt% Other**	*(FeO+CaO)/SiO_2*	*FeO/CaO*
S1	49.80	34.10	3.40	11.60	1.00	1.56	14.51
S2	51.05	29.64	18.88	0.32	0.13	2.36	2.70
S3	35.27	46.27	17.78	0.17	0.52	1.15	1.98

**SrO was detected in the precursor slags but it could not be quantified due to its low amount*

Table 2. Dopants added (wt%) to the samples.

Sample ID	CeO_2	*$CsNO_3$*	*$Sr(NO_3)_2$*	*$Eu(NO_3)_3$*	*Cs^+*	*Sr^{2+}*	*Eu^{3+}*	*NO_3^-*
AAM1	-	-	-	-	-	-	-	-
AAM2	-	1.0	0.1	1.0	0.68	0.04	0.45	0.93
AAM3	5.0	1.0	0.1	1.0	0.68	0.04	0.45	0.93

2.2. ***Nanoparticles synthesis***

The CeO_2 nanoparticles were synthesised using a modified precipitation-hydrothermal method (Fig. 1), as detailed in previous studies [29], [43], [44]. Cerium(III) ammonium nitrate ($(NH_4)_2Ce(NO_3)_6$ (Alfa Aesar 99.5%)) was dissolved in demineralised water at a concentration of 0.46 M while stirring. The precipitation of hydrous CeO_2 commenced with the addition of 5% ammonium hydroxide (Ammonia solution 25%, Merck). After stirring overnight, a light-yellow suspension was obtained. This suspension was then centrifuged and extensively washed with demineralised water to remove any residual ammonia.

Following the final wash, the solid was re-dispersed to a 5% concentration in demineralised water and subjected to hydrothermal treatment using a microwave digestion system (Speedwave Xpert, BERGHOF). The suspensions were heated to 180°C with a 40°C ramp and maintained at 180°C for 80 minutes. The resulting nanoparticles were centrifuged, dried at room temperature, and stored in dry conditions. An XRD analysis of the dry powders was conducted using a Rigaku Miniflex 600 diffractometer (results not shown). The crystallite size of the nanopowders was determined from the XRD pattern using an average of 8 selected peaks in the 2θ range between 25 and 80° with the Scherrer equation:

$$L = \frac{K\lambda}{\beta cos\theta} \quad (1)$$

where L is the size of coherently diffracting domains, K is the Scherrer constant (0.9 for spherical structures), λ is the incident X-ray wavelength (Cu K_α = 0.15406 nm), ϑ is the Bragg angle, and β is the peak full width at half maximum intensity. The crystalline size was estimated to be 2.6 nm on average, based on XRD measurements of several batches. SEM analysis of the nanoparticle-containing AAM samples revealed that the nanoparticles were aggregated in various sizes of agglomerates. To achieve a more even distribution of nanoparticles in the AAM samples, the produced nanopowder was ground using a planetary ball mill (PULVERISETTE 7 premium line, Fritsch) and then sieved through a 71 µm sieve.

2.3. *Sample Irradiation*

The irradiation of iron-rich AAM samples with a gamma dose of 6.51 MGy was carried out at the irradiation facility of CVŘ in the Czech Republic using a ^{60}Co source as described in [45]. The starting dose rate of the source was measured to be 1.4 kGy/h. The irradiation chamber was maintained at a constant temperature of 25°C. Due to the long-term nature of the measurement, the positions of the samples were not fixed and were changed over time, with the samples being in the tens of centimetres away from the source. The environment maintained ambient temperature and humidity.

2.4. *Up-Flow Percolation Test*

An up-flow percolation test was used to evaluate the samples' immobilization capacity in accordance with the CEN/TS 16637-3 standard [41]. Samples were dried at 40°C until constant mass in a lab oven after being cured for at least 28 days and after the irradiation period. They were then cooled down before being handled any further. Next, the samples were crushed until 45% and 100% of the test particle size was less than 4 mm and less than 16 mm, respectively. After, 90 g of the sample was placed within a glass column that measured 200 mm in length and 30 mm in inner diameter. On the top and the bottom of the column, filter paper (Schleicher & Schuell, nr. 595) was placed in order to keep sample particles from clogging the tubes and connectors. Viton® tubing with an inner diameter of 0.64 mm was used to connect the column's outlets. Distilled water was employed as the leachate solution. A volumetric peristaltic pump (IPC High Precision Multichannel Dispenser, Ismatec) was used to pump the leachate through the system at a flow rate of 0.096 ml/min. An illustration of the setup is shown in Fig. 1. After the column was saturated for 4 hours, a 64-hour equilibration interval was implemented. At pre-set intervals of 0.10 ± 0.02 l/kg, 0.10 ± 0.02 l/kg, 0.30 ± 0.05 l/kg, 1.00 ± 0.05 l/kg, 2.0 ± 0.05 l/kg, 3.0 ± 0.1 l/kg, and 5.0 ± 0.2 l/kg) seven eluate fractions were collected until a cumulative liquid over solid (eluate over sample portion in the column) ratio (L/S) of 11.5 ± 0.5 l/kg was reached. The pH and conductivity of the eluates were measured (MP225 pH Meter, METTLER TOLEDO) and (Portable Conductivity Meter, METTLER TOLEDO) after they were collected. The leaching tests were conducted at 20 ± 5 °C in a laboratory setting. The setup was cleaned with 0.1 M HNO_3 and distilled water prior to each leaching test. After each test was completed, the samples were dried at 80°C until they reached a consistent mass.

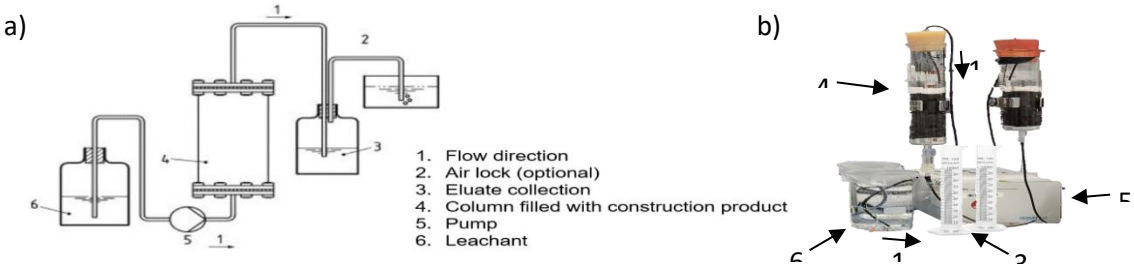

Fig. a) Illustration of leaching set-up ADDIN CSL_CITATION {"citationItems":[{"id":"ITEM-

2.5. *Characterisations*

2.5.1. SEM/EDS

Scanning electron microscopy (SEM) was carried out using a Thermo Scientific Quattro Scanning Electron Microscope fitted with an Energy-dispersive X-ray spectroscopy (EDS) XFlash 6/30 detector and an FEG electron source. Polished, non-coated cured samples were examined to compare the final microstructure of AAM mortars. Furthermore, mapping was created for particular samples.

To reduce surface roughness and provide a smooth surface for both SEM observation and nanoindentation testing, cured samples were cut plane-parallel using a water-cooled diamond saw, embedded in epoxy, and polished (AutoMet 250 Grinder-Polisher, Buehler) in accordance with Table 3. After polishing, the samples were disembodied from epoxy, fragmented and glued on the sample holder with a few drops of mounting adhesive (Crystalbond 509) for nanoindentation testing or SEM observation.

Table 3. Polishing procedure for SEM and Nanoindentation.

Polishing Material	*Grit (µm)*	*Duration (min)*
Sandpaper P-240	54.5	1
Sandpaper P-1200	15.3	1
Silicon carbine P-4000	2.5	3
Diamond paste 9	9	8
Diamond paste 3	3	8
Diamond paste 1	1	8

2.5.2. ICP- MS

Eluate solutions were analysed through ICP-MS (ElementXR, Thermo Fisher Scientific) to detect and quantify the eluate solutions. The elements under analysis included the dopant Cs, Sr, and Eu, as well as Fe, Al, and Na, the matrix's structural elements. Every aliquot was acidified until 1M HNO_3 was the final concentration. A function of L/S (7 eluate fractions) was used to evaluate the outcomes. Table 4 provides the detection limits (DL) for each elemental measurement. Ten spectra were gathered for every specimen, and each sample was examined three times. The reported leaching results are the average of these measurements and the errors are derived from the standard deviation. Because of the low Al content of slags S2 and S3, Al was not found in these samples.

Table 4. DL in µg/l for ICP-MS. Using the density of a 1M HNO3 solution, the DL was determined.

Element	*Fe*	*Na*	*Al*	*Cs*	*Sr*	*Eu*	*Ce*
DL in µg/l	2.8	7.1	1.41	0.014	0.14	0.014	0.014

2.5.3. Nanoindentation

In order to assess whether mortar composition, addition of dopant elements, and irradiation affect mechanical properties, we carried out nanoindentation tests to extract elastic modulus (E) and indentation hardness (H_{IT}) from the different phases identified in the samples. The sample microstructure and the presence of different components and phases result in a highly heterogeneous structure with complex mechanical responses, which makes the nanoindentation analysis particularly challenging. This aspect will be discussed further in the text.

We carried out load-controlled indentations using a nanoindenter (ASA nanoindenter from Alemnis GmbH) with a Berkovich (3-sided pyramid) diamond tip on sample composition AAM2_S1, AAM2_S2, AAM2_S2_IRR. The instrument was operated within an acoustic enclosure coupled to a vibration isolation platform. The system calibration was checked on a fused silica standard before and after the measurement campaign. For each sample, 2 rectangular grids 180 x 200 µm size, with 105 indentation points spaced by 20 µm each were carried out. Fig. 2 shows a representative selection of points of such grid on AAM1_S1 sample, with the indentation points circled in red for easy visualisation.

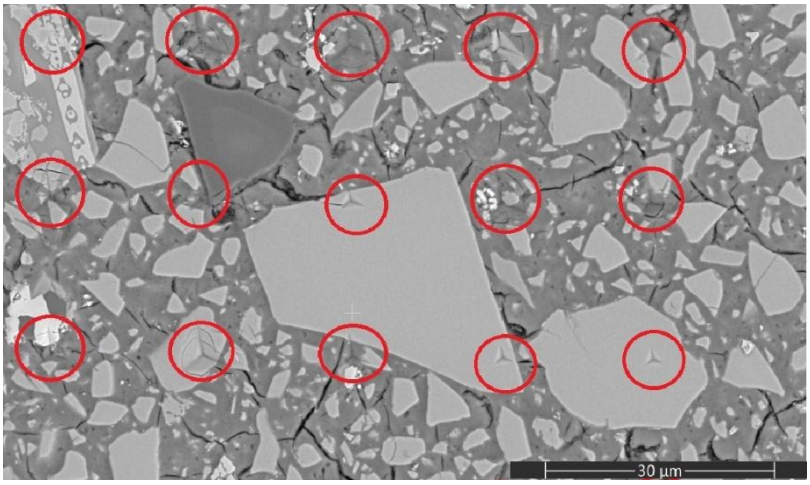

Fig. Selection of grid points (indentations circled in red) on sample AAM1_S1

We applied a trapezoidal loading diagram with a linear loading rate of 0.5 mN/s up to a maximum load of 10 mN. The maximum load was kept constant for 40 s to allow the material to creep, followed by the unloading step at 0.5 mN/s. During unloading, an additional 60 s load step at 1 mN was applied to allow for thermal drift correction.

Elastic modulus E and indentation hardness H_{IT} are derived from the experimental load (P) – displacement (h) curves with the Oliver–Pharr method [46] under the assumption of an elastic recovery during the unloading phase of the indentation. Details on the extraction of E and H_{IT} from experimental curves are provided in the Appendix.

After each indentation run, the samples were visually inspected with both optical microscope and SEM in order to localise and index the indents according to the landing area. Through indexing, it was possible to associate each experimental load-displacement curve to the corresponding indent in the SEM image. The indents were assigned to an island (unreacted slag) if the island area was bigger than 3 times the area of the imprint. Otherwise, they were assigned to the matrix. Indents landing on cracks or voids, as well as on the edges of the islands, where discarded (see chapter 3.2 about microstructure).

2.5.4. Image Analysis

For each sample, a single image was captured at 1500x magnification using a Scanning Electron Microscope (SEM), analysed with Image Pro v.10 software (Media Cybernetics Inc., USA), and a custom image analysis method was developed to evaluate the images. The objective was to characterise the Fe-rich polymers by assessing the number and size of islands, the surface area covered by the matrix, and the presence of voids and cracks within the matrix. To achieve this, each image was spatially calibrated, and a multi-thresholding technique was applied to distinguish three regions: voids and cracks (black areas), the matrix (dark grey areas), and islands (light grey areas). For each sample, the

following features of the islands were measured and reported as average values with standard deviations: area, average diameter, perimeter and the number of islands. Additionally, the total area covered by each surface type was calculated.

3. Results

To gain a better understanding of the leaching of structural elements as well as contaminants from AAM samples, the results of the up-flow percolation tests were analysed. The immobilisation capacity of contaminants Cs, Sr, Eu were evaluated under normal conditions without any prior handling of the samples (sample series AAM2), after irradiation (AAM2_IRR series) and with the presence of CeO_2 nanoparticles (AAM3 sample series). The effect of the irradiation on the morphological, chemical and mechanical properties was examined with SEM, EDX mapping, image analysis and nanoindentation techniques,

3.1. *Leaching*

Fig. 3 reports the evolution of the pH of the eluates leached throughout the up-flow percolation test; the results are also shown in Appendix Table A1. For the investigated samples, the overall eluate pH trends were relatively comparable. After an increase in the pH to the 5^{th} -6^{th} eluate, the pH seemed to stabilize, except for samples AAM2_S3 and AAM3_S2 as well as for the irradiated versions of AAM2 samples which exhibit a slight decrease in pH until the end of the experiment.

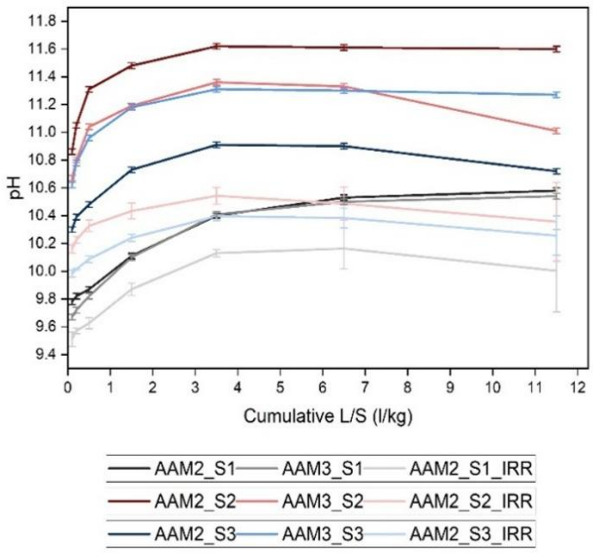

Fig. Eluate pH in relation to cumulative L/S (l/kg). The three distinct slag composition samples are colour coded. S1 is represented by grey, S2 by red, and S3 by blue.

Considering samples made with slag S2, AAM2_S2 had an overall higher level of pH throughout the whole experiment than sample AAM3_S2. Considering samples with slag S3, AAM2_S3 had a lower overall pH level than AAM3_S3. Samples made with slag S1 had a lower initial pH, as well as a lower final pH, relative to other slag-based samples. The irradiated samples showed an overall lower pH progression throughout the experiment compared to their respective non-irradiated pairs.

The cumulative release for Fe, Na, Al, Cs, Sr and Eu is shown in Fig.4 and in Fig. 5 (in mg/kg of sample dry mass) as a function of cumulative L/S. It is evident that the use of different slags as well as the addition of the CeO_2 nanoparticles and irradiation had an impact on the leaching behaviour of different elements in the samples.

The cumulative release of Fe showed irregular patterns and is relatively low across all samples. The irradiated versions show a decrease in Fe release in comparison with the non-irradiated counterparts, with AAM2_S1_IRR peaking at 0.263 mg/kg, AAM2_S2_IRR at 0.329 mg/kg, and AAM2_S3_IRR at 0.199 mg/kg (5.7, 5.5 and 3.1 times lower than their non irradiated counterparts respectively).

Na shows significant cumulative release, much higher than other elements, with irradiation generally increasing Na release. The irradiated samples exhibit a pronounced increase in release due to

irradiation with samples AAM2_S1_IRR, AAM2_S2_IRR and AAM2_S3_IRR exhibiting 1.8, 1.3 and 1.7 times higher Na release than their non irradiated counterparts respectively.

Al release is relatively low across the samples, with not all samples containing measurable Al levels. In particular, the Al content in slags S2 and S3 is under the ICP-MS detection limit. For S1 based samples, the Al content is measurable, and it is observed that for AAM2_S1_IRR, Al release peaks at 3.3 mg/kg which is 2.5 times lower than the Al release in AAM2_S1 which reaches up to 8.25 mg/kg.

a)

b)

c)

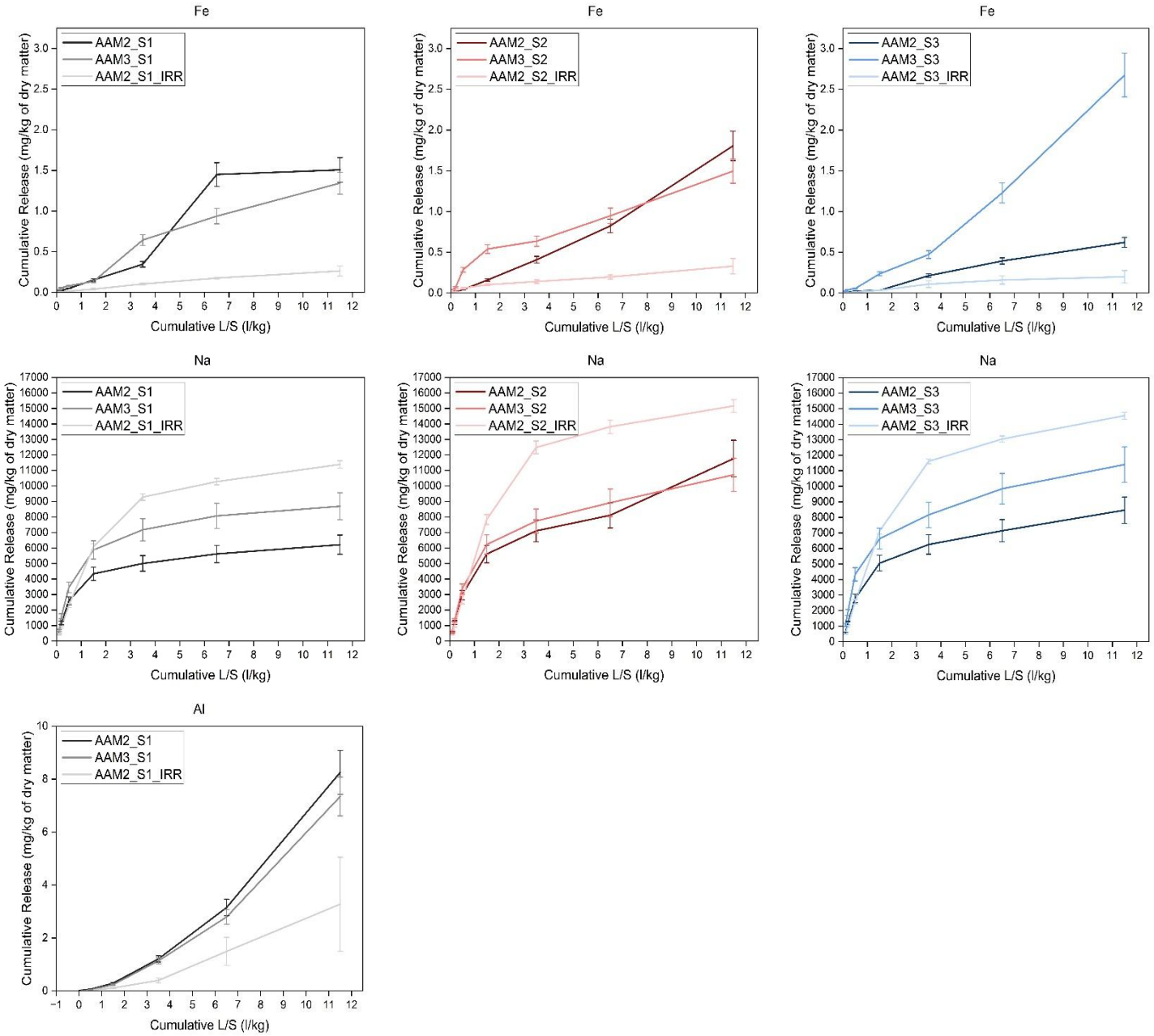

Fig. Cumulative release of a) iron, b) sodium, c) aluminium in function of the cumulative L/S ratio (l/kg).

Cs release is moderate and shows variation across samples, with irradiation impacting the release behaviour. The irradiated samples show a higher Cs release with irradiation, with the Cs release in AAM2_S1_IRR ranging from 6.6 mg/kg to 96.0 mg/kg, AAM2_S2_IRR from 10.6 mg/kg to 196.8 mg/kg, and AAM2_S3_IRR from 14.1 mg/kg to 268.0 mg/kg, overall, 0.9, 0.5 and 0.8 lower total release in comparison to their irradiated counterparts.

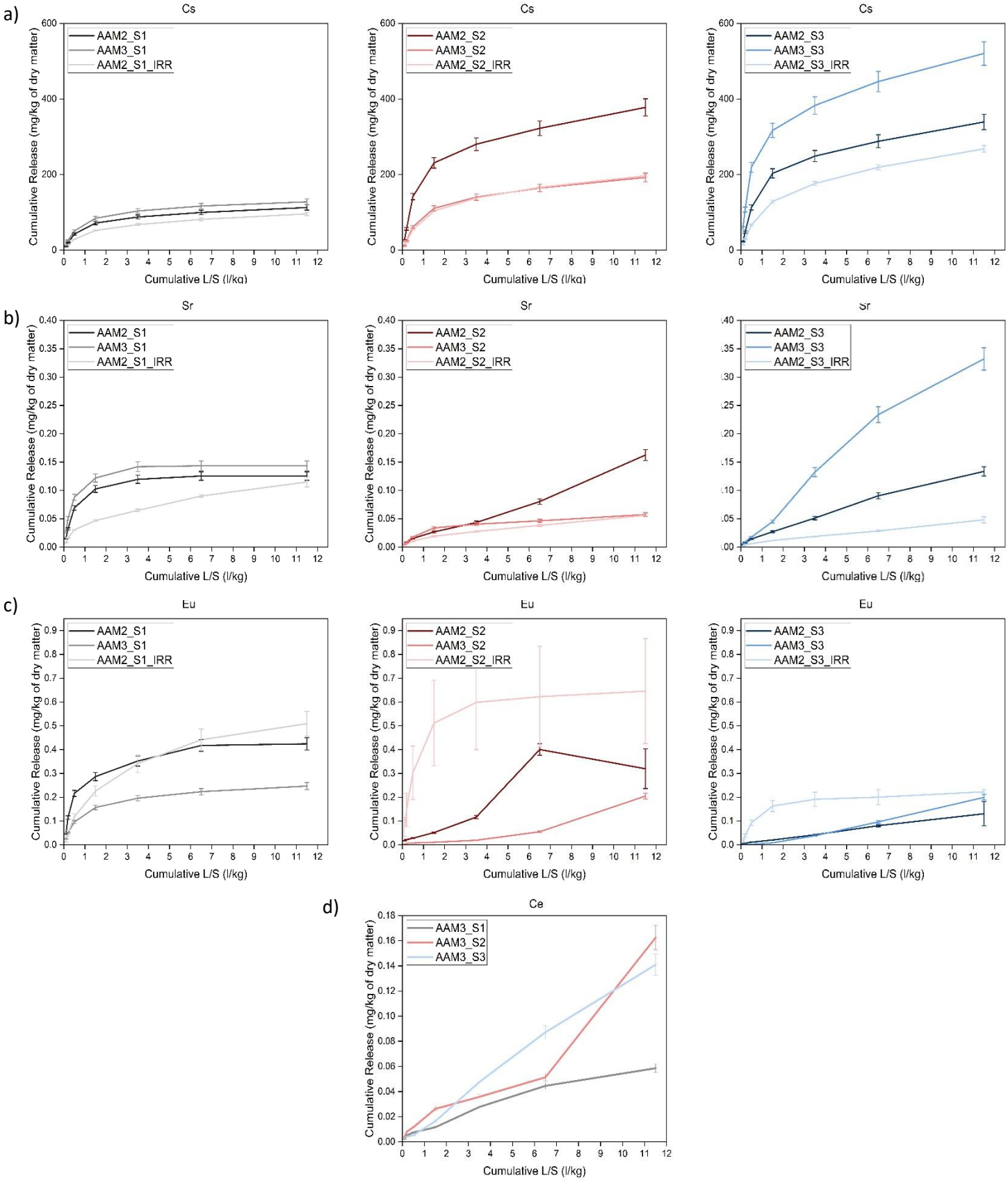

Fig. Cumulative release of a) caesium, b) strontium, c) europium and d) cerium in function of the cumulative L/S ratio (l/kg).

Sr release is low to moderate, with irradiation altering the release patterns. Samples AAM2_S1, AAM3_S1, AAM3_S2 and AAM3_S3 displayed a progressive increase with respect to the L/S showing a similar evolution pattern. In samples AAM2_S2 and AAM2_S3, Sr showed a different release pattern, following a more exponential release trend. The irradiated samples show cumulative release up to 0.115 mg/kg for AAM2_S1_IRR, 0.056 mg/kg for AAM2_S2_IRR, and 0.048 mg/kg for AAM2_S3_IRR, 0.9, 0.3 and 0.4 times less than in samples AAM2_S1, AAM2_S2 and AAM2_S3 respectively.

Eu release is low to moderate, with significant variation across samples and noticeable effects due to irradiation. Samples AAM2_S1 and AAM3_S1 demonstrated a continuous rise in their cumulative release relative to the L/S ratio, exhibiting a comparable pattern of progression. In samples AAM2_S2, AAM3_S2, AAM2_S3 and AAM3_S3, Eu exhibited a release pattern characterized by a more pronounced exponential trend. The irradiated samples show a cumulative release peaking at 0.509 mg/kg for AAM2_S1_IRR, 0.646 mg/kg for AAM2_S2_IRR, and 0.223 mg/kg for AAM2_S3_IRR, which was 1.2, 2 and 1.7 times higher than in samples AAM2_S1, AAM2_S2 and AAM2_S3 respectively.

The release of Ce across all samples seems to be similar to the release trends for Fe in each respectable sample showing irregular patterns.

The relative release of the dopants Cs, Sr, Eu and Ce are shown in Fig. 6. The relative release was calculated based on the amount (mg) of the element present in the testing portion at the start of the percolation test and the total amount (mg) that was released in all the eluates collected during the experiment. Samples AAM2_S1 and AAM3_S1 performed generally better than the other samples

having the lower relative release (%) for Cs being lower than 2%. In all cases, the relative release for Sr was under 0.08%, for Eu lower than 0.009% and for Ce lower than 0.0003%.

The release rates of several elements from the AAM2 samples—both irradiated and non-irradiated—are shown in Table 5 and Table 6 with notable variations noted for each element. All samples showed a considerable reduction in Fe release following irradiation; reductions of 83%, 82%, and 68% for AAM2_S1, AAM2_S2, and AAM2_S3 respectively, which indicates a significant drop in iron's solubility

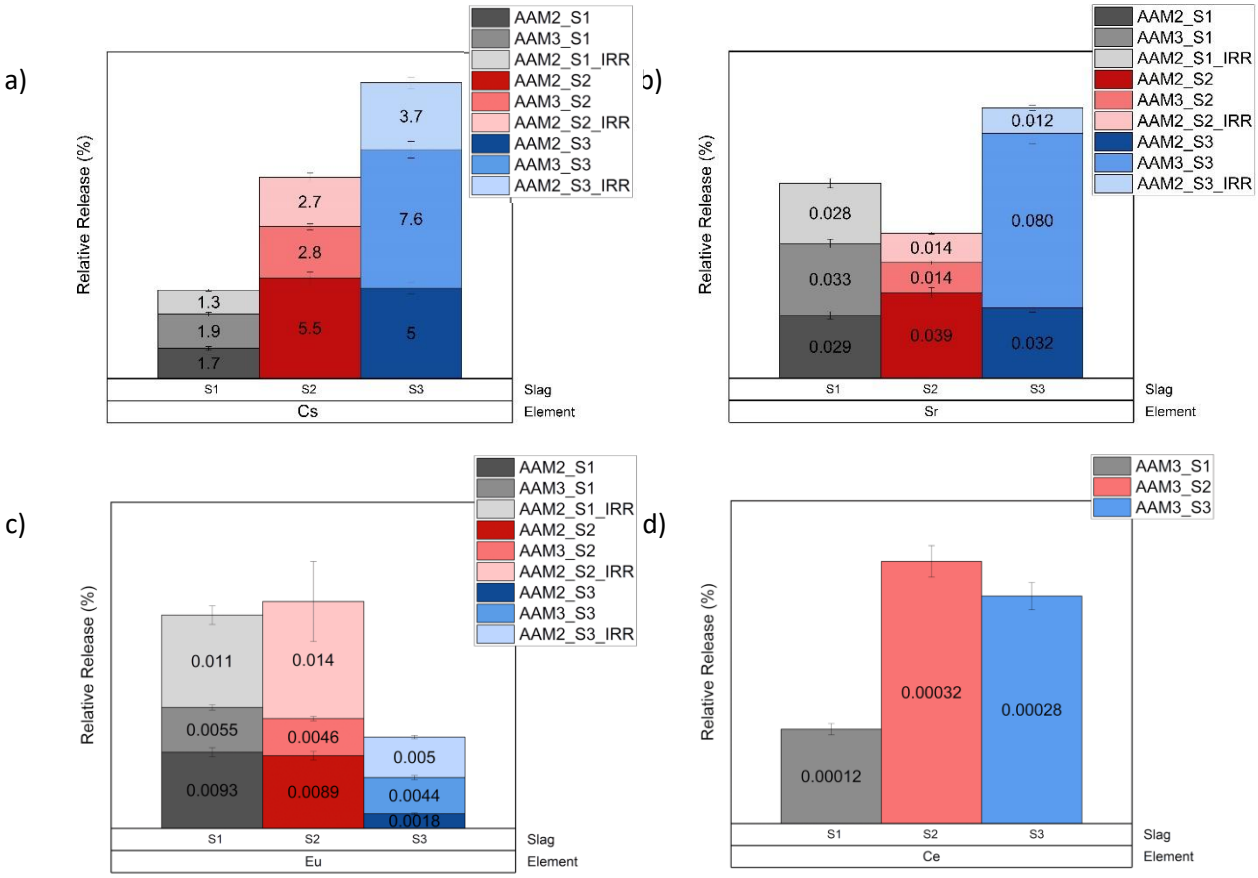

Fig. Relative release for a) caesium, b) strontium, c) europium and d) cerium.

or mobility after irradiation. On the other hand, following irradiation, Na release rose significantly, increasing by 83%, 29%, and 72% for AAM2_S1, AAM2_S2, and AAM2_S3, respectively, suggesting an increase of salt leaching or solubility. The release of Al, which was exclusively recorded for AAM2_S1, decreased by 60% following irradiation, suggesting enhanced stability. Following radiation, the release of Cs dropped for all samples; for AAM2_S1, AAM2_S2, and AAM2_S3, the reductions were 15%, 48%, and 21%, respectively, indicating a decrease in mobility. The release of Sr also steadily declined following irradiation; reductions of 2.9%, 66%, and 64% for AAM2_S1, AAM2_S2, and AAM2_S3 respectively, indicated lower mobility. With increases of 22%, 61%, and 176% for AAM2_S1, AAM2_S2, and AAM2_S3, respectively, Eu release showed considerable heterogeneity.

Table 5. Total elemental release rates from AAM2 samples without and with irradiation.

Table 6. Total release of elements (mg/kg) in samples doped with CeO_2 nanoparticles.

Sample	*Fe*	*Na*	*Al*	*Cs*	*Sr*	*Eu*	*Ce*
AAM3_S1	1.3 ± 0.1	8700 ± 870	7.3 ± 0.7	130 ± 8	0.14 ± 0.01	0.25 ± 0.01	0.060 ± 0.0
AAM3_S2	1.5 ± 0.1	11000 ± 1100	-	190 ± 10	0.057 ± 0.003	0.20 ± 0.01	0.16 ± 0.0
AAM3_S3	2.7 ± 0.3	11400 ± 1100	-	520 ± 30	0.33 ± 0.02	0.20 ± 0.01	0.14 ± 0.0

			Fe	*Na*	*Al*	*Cs*	*Sr*	*Eu*
AAM2_S1	*Non-Irradiated*	*mg/kg*	1.5 ± 0.2	6200 ± 620	8.3 ± 0.8	110 ± 7	0.12 ± 0.01	0.42 ± 0.03
	Irradiated		0.26 ± 0.6	11400 ± 240	3.3 ± 1.8	96 ± 4.7	0.11 ± 0.01	0.51 ± 0.05
	Difference	*%*	-83	83	-60	-15	-2.9	22
AAM2_S2	*Non-Irradiated*	*mg/kg*	1.8 ± 0.2	12000 ± 1200		380 ± 25	0.16 ± 0.01	0.40 ± 0.02
	Irradiated		0.33 ± 0.10	15160 ± 400		200 ± 3.5	0.056 ± 0.002	0.7 ± 0.2
	Difference	*%*	-82	29		-48	-66	61
AAM2_S3	*Non-Irradiated*	*mg/kg*	0.60 ± 0.06	8500 ± 850		340 ± 20	0.13 ± 0.01	0.080 ± 0.005
	Irradiated		0.20 ± 0.08	14500 ± 230		270 ± 8.8	0.048 ± 0.005	0.22 ± 0.01
	Difference	*%*	-68	72		-21	-64	176

3.2. ***Microstructure***

Different islands were visible following EDX analysis, and they represent portions of unreacted slag. When compared to the darker matrix part, these islands had a notably lower Na mass (%) and a greater Fe mass (%). Fig. 7 shows SEM micrographs of the AAM1_S1, AAM2_S1 and AAM3_S1 samples. In all cases, distinct islands were visible which possibly correspond to parts of unreacted slag, since the Na mass (%) is visibly lower and the Fe mass (%) is higher than on the darker matrix portion, after performing EDX analysis. In all cases the 'islands' (indicated in Fig. 7) also exhibited scattered spots of higher Fe concentration which appear to be brighter than the rest of the 'island'. This could be attributed to the synthesis of the slag and the homogenisation process, while mixing the starting materials. Cracking was visible in all samples, the origin of that could not be associated directly with any specific process at this point of this work. For sample AAM3_S1 CeO_2 aggregates were visible.

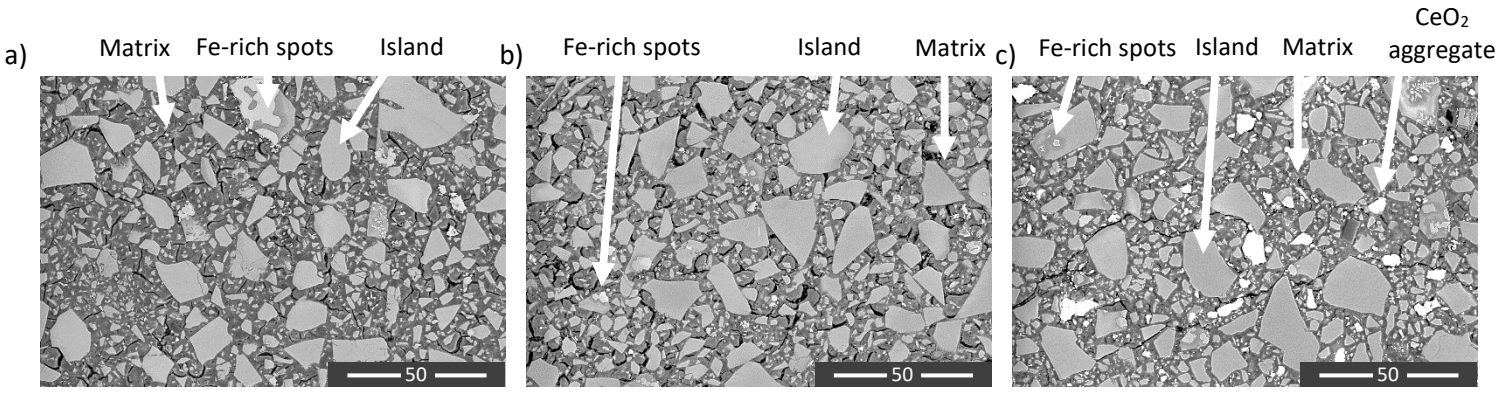

Fig. Secondary electron micrographs of the inorganic polymers a) AAM1_S1, b) AAM2_S1 and c) AAM3_S1 where the lighter areas are CeO_2 nanoparticles. The scale is measured in μm.

These aggregates showed Eu accumulations which was also seen in the EDX mapping in Fig. 8. There is no available data for Sr, since it was below detection limit.

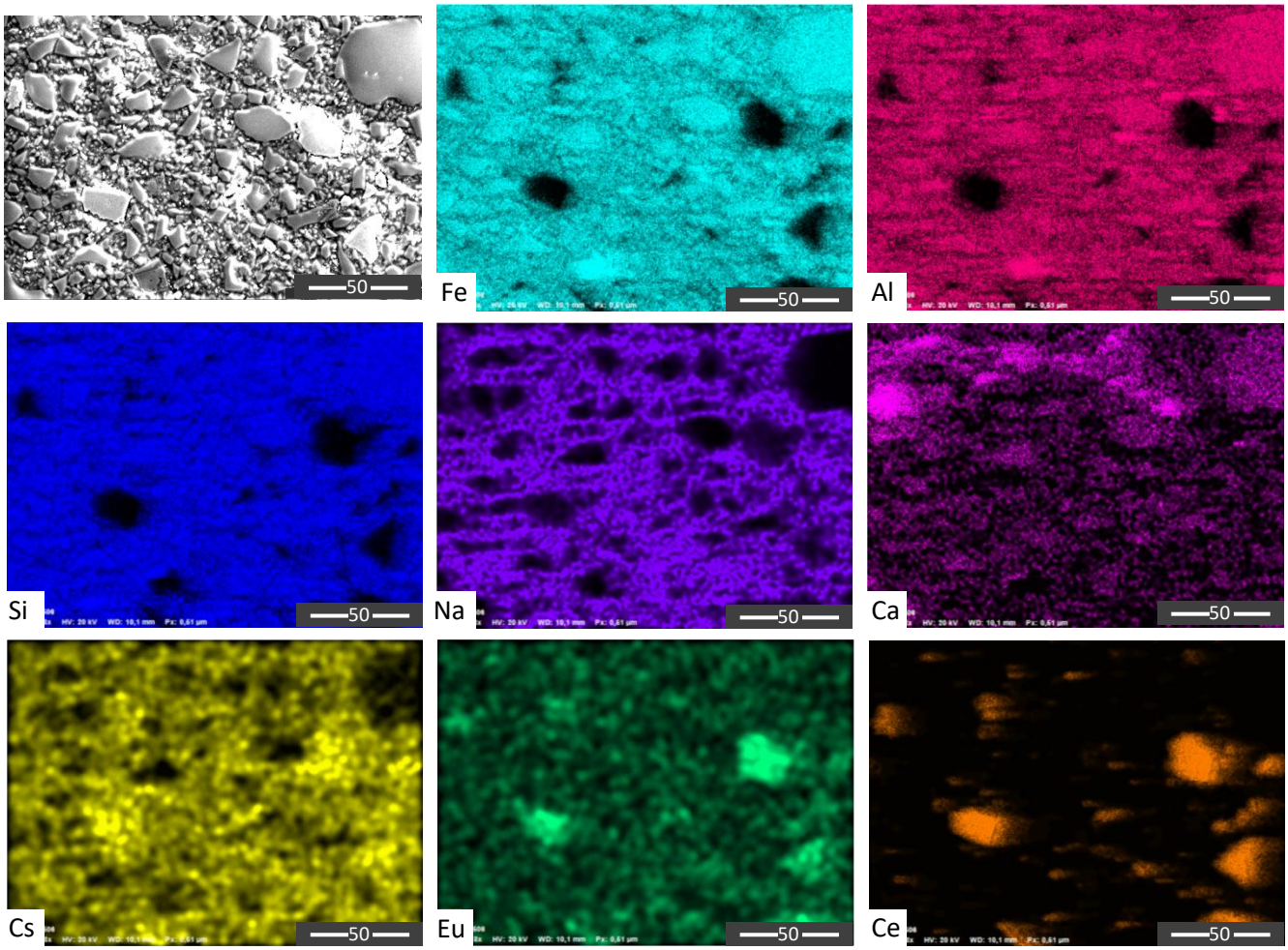

Fig. EDS-Mapping analysis of polished sample AAM3_S1. The scale is measured in μm.

The findings of the EDX analysis, which was performed on the different regions of the samples, are shown in Table 7. There are several differences between the AAM2_S1 and AAM2_S1_IRR samples in the matrix and island regions. Fe concentrations in the non-irradiated (30.8% ± 0.8%) and irradiated

(30.7% ± 0.9%) samples are about the same in the matrix. Nonetheless, in the Fe-rich islands, the irradiated sample exhibits a slight increase in Fe content as a result of irradiation, with a greater Fe content (47.9% ± 4.8%) than the non-irradiated sample (42.3% ± 1.0%). While Fe-rich islands display identical Na levels, the irradiated sample's normal matrix had lower sodium (Na) concentrations (2.9% ± 0.2%) than the non-irradiated sample's (3.5% ± 0.3%), indicating sodium depletion from irradiation. Irradiation has little effect on silicon (Si) concentrations in any region, with a few exceptions.

The matrix's Ca concentration level is somewhat higher in the irradiated sample, but noticeably lower in the Fe-rich islands, suggesting that irradiation lowers Ca concentration in these areas. The irradiated sample's Fe-rich islands exhibit a considerable decrease in Al concentration compared to the matrix, indicating that irradiation reduces the Al concentration in these places. The minor changes in Cs and Eu concentrations throughout both regions suggest that radiation does not impact them much. Overall, decreased Al and Ca concentrations and increased Fe concentration on Fe-rich islands, combined with minor Na depletion in the matrix phase, are the most notable effects of irradiation.

Table 7. Normalised mass concentration (%) for structural and doping components as determined by EDX analysis performed on various sample sections.

	AAM2_S1_IRR			AAM2_S1			AAM3_S1			
	Matrix	Island		Matrix	Island		Matrix	Island		Nanoparticles
		Normal	Fe rich		Normal	Fe rich		Normal	Fe rich	
Fe	30.7 ± 0.9	34.9 ± 0.7	47.9 ± 4.8	30.8 ± 0.8	35.4 ± 0.3	42.3 ± 1.0	31.2 ± 1.8	35.0 ± 0.5	45.74 ± 0.06	12.2 ± 1.0
Na	2.9 ± 0.2	0.64 ± 0.03	1.0 ± 0.4	3.5 ± 0.3	0.90 ± 0.09	1.00 ± 0.07	3.1 ± 1.5	2.7 ± 2.9	0.70 ± 0.04	2.1 ± 0.6
Si	16.3 ± 0.4	15.8 ± 0.5	8.4 ± 3.5	16.6 ± 0.3	16.0 ± 0.3	9.3 ± 1.2	15.6 ± 0.3	15.7 ± 0.1	7.0 ± 0.9	8.2 ± 0.4
Ca	2.7 ± 0.7	3.0 ± 0.1	1.1 ± 0.4	2.5 ± 0.4	2.90 ± 0.07	1.6 ± 0.3	2.2 ± 0.3	2.75 ± 0.06	1.0 ± 0.2	2.1 ± 0.1
Al	5.8 ± 0.3	6.4 ± 0.1	6.2 ± 2.0	5.7 ± 0.3	6.6 ± 0.2	10.2 ± 1.0	5.2 ± 1.3	4.6 ± 2.8	10.1 ± 1.2	2.6 ± 0.6
Cs	1.2 ± 0.1	0.25 ± 0.04	0.3 ± 0.1	1.2 ± 0.1	0.27 ± 0.02	0.3 ± 0.03	0.9 ± 0.3	0.25 ± 0.04	0.18 ± 0.01	0.6 ± 0.1
Eu	0.7 ± 0.2	0.27 ± 0.05	0.31 ± 0.06	0.7 ± 0.1	0.30 ± 0.04	0.3 ± 0.02	0.50 ± 0.09	0.25 ± 0.03	0.20 ± 0.02	2.2 ± 0.3
Ce	-	-	-	-	-	-	3.6 ± 1.7	1.2 ± 0.2	0.76 ± 0.03	45.4 ± 2.2

3.3. ***Image Analysis***

In Fig. 9 the original, segmented and clustered images for each type of sample are displayed. Notably, AAM2 samples exhibit the highest presence of voids and cracks, a finding corroborated by the image analysis results. As shown in Table 8, in fact, voids and cracks cover 9.86% and 10.33% of the surface area in AAM2_S1 and AAM2_S1_IRR respectively. These values are assessed by grouping pixels according to software assigned grey level thresholds (image segmentation process). Pixels groups are

therefore associated to a phase (island, matrix or void/craks) and then counted to assess the area covered by the phase.

To determine whether there were statistically significant differences between the samples, the area, diameter, and perimeter values within each class of island dimensions were analysed using a one-way ANOVA test followed by a multiple range test. Although the AAM1_S1 sample had the smallest total area occupied by islands, these analyses were conducted for all samples (Appendix Table A3). Sample AAM2_S1 exhibited unique characteristics, showing the smallest island dimensions in one size range

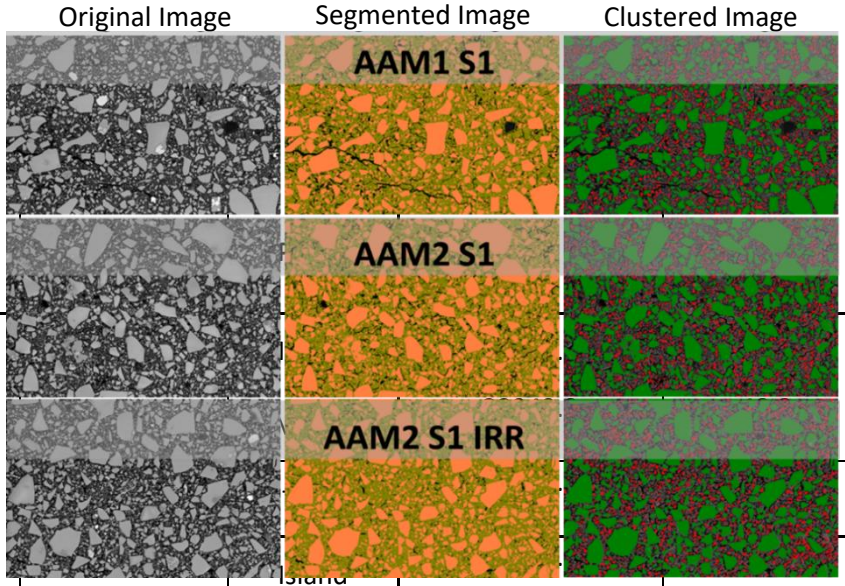

Fig. Original SEM images and thresholded images of all the AAMs.

Total Image Surface (µm²)					% Cracks/voids
48616.2	AAM2_S1	Island	43824.3	90.1	7.15
		Matrix			9.86
		Total			
	AAM2_S1_IRR	Island	22549.4	46.4	10.33
		Matrix	21046.9	43.3	
		Total	43596.3	89.7	

while displaying intermediate behaviour in another, setting it apart from the other analysed samples.

Table 8. Surface analysis results.

3.4. ***Nanoindentation***

For the purpose of our nanoindentation analysis, as supported by SEM images, we observe big islands of unreacted slag surrounded by smaller ones with the matrix phase filling the spaces in-between.

As one can see in (Fig. 2), a small number of indentations landed on big islands, whereas the majority landed in the matrix, in regions that are mostly occupied by small islands.

At the selected 10 mN maximum load, the maximum indentation depth *h* for the indents landing on the big islands is in the range of 200-500 nm, whereas for the indents landing on the matrix, the range

is 600-800 nm. The residual imprint of the indentation has a characteristic length (side of the triangle) of approx. 2-3 µm for both phases.

Fig. 10 presents typical experimental load-displacement curves where one can distinguish the different depths associated with the landing sites (big islands and matrix). Indentations landing on cracks or porosities have been discarded.

A quite consistent number of experimental curves showed load drops on the loading section (some can be seen in Fig. 10. However, the unloading section does not present load drops and shows elastic

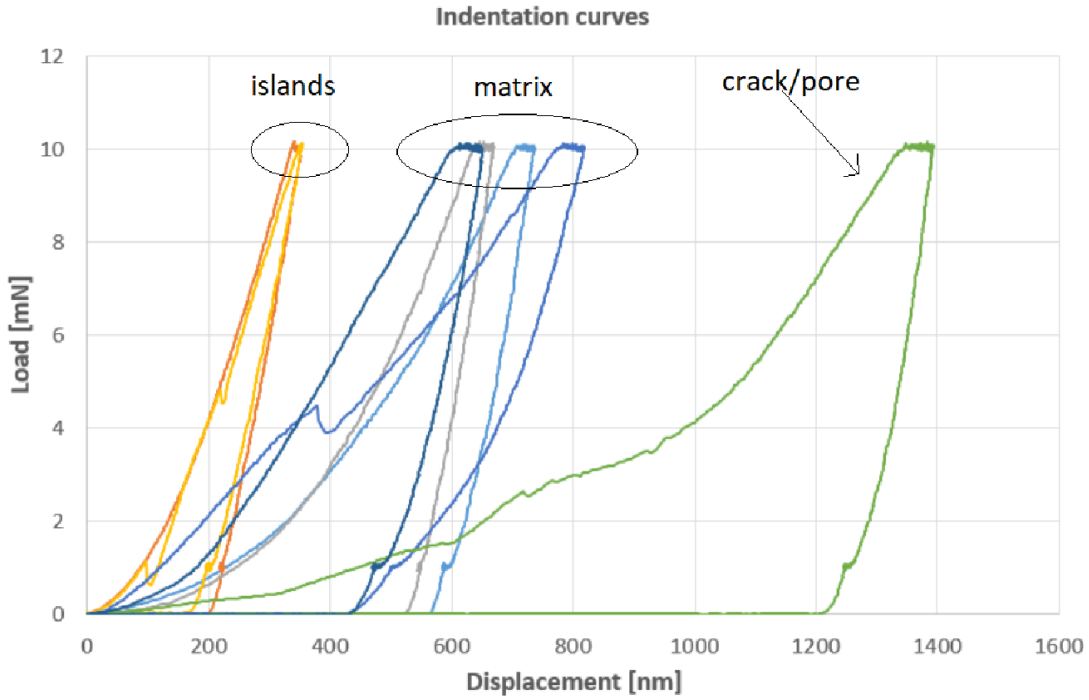

Fig. Selection of representative load-displacement curves on the AAM1_S1 sample.

recovery, as required for the validity of the Oliver-Pharr method. Load drops are probably due to surface or sub-surface cracks developing during the loading phase. However, most of the residual indent under SEM observation did not show any superficial cracks. Also, no material accumulation at the edges of the residual indent (pile-up) was observed.

For each nano-indentation test, H_{IT}, E and maximum depth were recorded, as detailed in the Appendix. To assess whether the distribution of each feature was comparable across the samples, a density plot

statistical analysis was performed. Fig. 11 and Fig. 12 display the density plots for E, H_{IT} and maximum depth (h_{max}) for the matrix and island phases, respectively.

In the matrix phase, the distributions of the selected parameters follow a similar trend, except for the

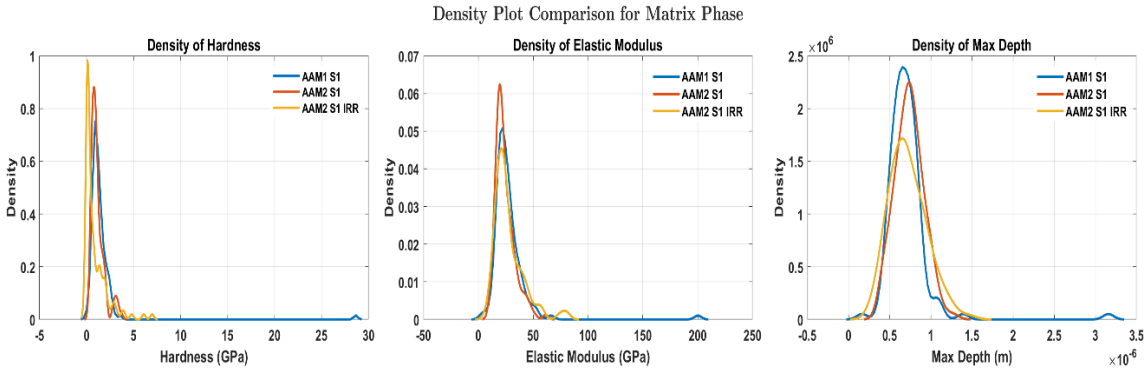

Fig. Density plot of all nanoindentation features for the Matrix phase.

density plots of hardness, which show significant shifts, particularly from the average values. This deviation could be attributed to phase heterogeneity.

In contrast, the density plots for the island phase reveal more pronounced differences. The most notable variation is in the hardness distribution of the islands, which exhibits a completely different

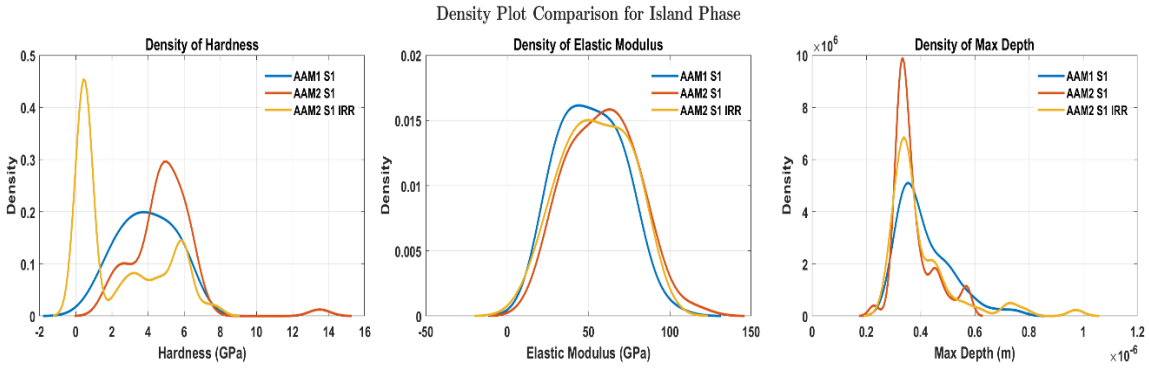

Fig. Density plot of all nanoindentation features for the Island phase.

trend and average values compared to the other samples. Interestingly, the AAM1_S1_IRR distribution appears to have a potential tri-modal pattern, in contrast to the bimodal distribution observed in the AAM2_S1 sample, and the Gaussian distribution seen in the AAM1_S1 sample.

The results for the two different sample phases are found in Appendix Table A1, the hardness of the AAM2_S1_IRR sample is the lowest and is statistically different from all the others.

It is important to note that both H_{IT} and E exhibit large standard deviations, as further illustrated by the box plots in Appendix figures Fig. A3 and Fig. A4. When standard deviations are high, it becomes challenging to determine whether the average values reflect true differences in mechanical properties among the samples. To address this, a one-way ANOVA test followed by a multiple-range test was conducted on the H_{IT}, E, and maximum depth values (Appendix Table A1) to evaluate any statistically significant differences between samples. In table A2 of the Appendix superscript letters next to the mean values for H_{IT}, E, and maximum depth represent the results of the ANOVA test, indicating where

statistically significant distinctions exist among the samples. When different letters appear next to the mean values, it suggests a statistically significant difference.

Notably, the greatest statistical differences were observed for the H_{IT} values in the Island phase, where all samples differed from each other, with sample AAM2_S1 displaying the lowest value. A similar trend was observed in the Matrix phase, although in this case, sample AAM2_S1 exhibited some similarities with the other two samples concerning the H_{IT} value.

4. Discussion

Slag S1 has a higher Al content compared to the other two selected slags. The surplus of negative charge created when Al^{3+} substitutes Si^{4+} in the AAM network needs to be balanced by more positive charged ions, in this case Na^+, meaning less Na^+ available to be released (for exchange with H^+), which possibly explains the lower pH levels shown by samples AAM2_S1, AAM3_S1 and AAM2_S1_IRR [12], [47]. The rise of the pH (Fig. 3) during the first stages of the column experiment can be attributed to the dissolution of sodium, which increases the ionic strength of the solution decreasing the activity of H^+ ions, or to the dissolution of NaOH which is present in the activator, freeing OH^- anions. As the experiment proceeded the dissolution rate decreased, explaining the smaller variations in the pH towards the end of the procedure.

Earlier studies demonstrated that caesium ions (Cs^+) acted as charge-balancing cations within the aluminosilicate framework and played a crucial role in the geopolymerization process [48]. The increased presence of Al in slag S1, as mentioned above, would require more positive charge-balancing ions. This could explain why the retention of Cs was enhanced for samples AAM2_S1, before and after irradiation, and AAM3_S1 as well as lower leaching of Na, forming a stronger ferrosilicate network than the rest of the samples. This is also shown in Table 5 and Table 6. It is speculated that Ce can interact with Fe during the formation of the AAMs and displays a similar release pattern to Fe in the samples. Further analysis is needed in order to understand this occurrence better.

The cumulative release (Fig.4 and Fig. 5) observed for Na and Cs in all samples, Sr for AAM2_S1, AAM3_S1, AAM3_S2 and AAM3_S3 and Eu for samples AAM2_S1 and AAM3_S1 is characterized by a gradual increase in the concentration of element release that will potentially result in a stabilized concentration. Its slow rise suggests constraints from solid-phase availability, diffusion kinetics, or obstacles within the matrix, which eventually reach equilibrium, resulting in a constant leaching rate. On the other hand, the exponential release recorded for Sr in samples AAM2_S2 and AAM2_S3, Eu in AAM2_S2, AAM3_S2, AAM2_S3 and AAM3_S3 and Al in samples AAM2_S1 and AAM3_S1, suggests a swift release of the initially accessible reservoirs, and entails a rapid escalation in the rate of element release over the course of the experiment.

The presence of CeO_2 nanoparticles seems to have been beneficial in the samples made with slag S2, since the release of Cs, Cr and Eu showed to be lower than in their absence. The exact opposite was observed for samples made with slag S3 while in the case of slag S1 they did not seem to have a clear impact except for Eu.

The results of the leaching study in the samples after irradiation suggest that radiation tends to increase the mobility of Na and Eu while improving the immobilization of Fe, Al, Cs, and Sr inside the matrix. These findings demonstrate the various ways that gamma irradiation affects various components in alkali-activated materials. Radiolysis occurs during irradiation, ionizing water molecules. Electronic excitations and ionization result in the formation of relatively stable primary products (H_2, H_2O_2, H^+, and OH^-), or unstable free radicals (e−aq, H, OH) [49]–[51]. This process may

acidify the leachates lowering the pH, with respect to the pH of the leachates derived from non-irradiated samples. Irradiation significantly increases the release of Na in the early eluates. Cs release is generally lower in irradiated samples compared to non-irradiated samples. Other elements like Eu, and Sr show varied responses to irradiation, with both increases and decreases observed. Multiple studies have been made regarding the effect of gamma irradiation on Fe. The oxidation of Fe occurs via the irradiation induced formation of strong oxidants (e.g. H_2O_2): the oxidation state goes from 2+ to 3+ [52], [53]. Tetrahedral Fe^{3+} is incorporated into the network of the inorganic polymer matrix [54], [55], which explains the lower leaching rates in the irradiated samples.

The main difference between the three selected slags is the higher concentration of Al in S1. The release of Al is not shown in the results for samples with slags S2 and S3 since it was below detection limits. A high Cs concentration is related to a high Na concentration in all three series (S1, S2, S3), which can be explained by the fact that both Cs and Na are water-soluble elements. It should be considered that the traces of SrO in the slags, might influence the leaching results of Sr in the samples. Some of the leached Sr may be derived from the slag, rather than exclusively due to the addition of $Sr(NO_3)_2$ in the samples.

Salas et al. [56] evaluated the potential release of hazardous trace elements from blast furnace slag-based AAM samples. They used two different leaching tests to assess the elemental release of incorporated agro-industrial waste in AAMs, one designed to study the leaching from the surfaces of monolithic construction products, and one designed for granular construction products the up flow percolation test that is used in this work as well [41]. They found that AAMs effectively immobilise trace elements, resulting in leaching values that are below the inert waste acceptance criteria for both monolithic and granular forms. The leaching behaviour of the materials varies based on their form (monolithic vs. granular) and shows different long-term leaching behaviour depending on their composition but both tests ultimately showed that the retention ability of the AAM samples was efficient and compliant to soil regulations. Giels et al. [57] performed similar studies on the leaching behaviour of elements from inorganic polymers made from iron-rich slags using cascade and column leaching tests. Their results indicated that elements such as Mo, As, P, V, and Sb showed weak immobilization (1-50% released) in neutral pH leachates, due to their anionic nature, while Fe, Zn, Mn, Mg, Cu, and Ba demonstrated significant immobilization (<0.2% released) due to adsorption on the inorganic polymer matrix. The leaching behaviour studied in this work aligns well with the findings of these studies [56], [57] validating the chosen methodological approach. Furthermore, the observed relationships between pH evolution and elemental release rates are in good agreement with the mechanisms proposed by Salas et al. [56], supporting the reliability of our chosen testing protocol.

When it comes to immobilizing radioactive waste, AAMs hold great potential, especially when it comes to low-charged cationic species like Cs and Sr. However, further research and binder chemistry improvement may be necessary to fully understand how well AAMs immobilize metals with high oxidation states, like Eu. The basic mechanics of the interaction between radionuclides and AAMs, as well as the long-term performance of these materials under irradiation circumstances, are the main topics of ongoing research [58].

Nanoindentation has been developed for homogeneous materials. When indenting heterogenous materials such as AAMs, a number of additional hypotheses taking into account the lengths scale of the different phases present need to be made [59]. A generally accepted rule of thumb, derived by nanoindentation experiments with thin films on substrates, states that the maximum penetration depth to which an indentation test can produce reliable hardness measurements is around 10 % of the film thickness [60]. Beyond that, the substrate's mechanical response affects the film hardness value. Often, by analogy with the thin film case, researchers extend this rule to bulk heterogeneous

materials, where other phases act as a substrate, and to other mechanical properties including elastic modulus.

In consideration of the 10% rule, we assume that the distribution of small islands dispersed in the matrix around the indent is going to contribute to the mechanical response of the matrix over a range of 10 times the maximum indentation depth (i.e. 8 μm for the composite matrix and 5 μm for the big islands). In other words, the volume probed by the indentation is 10 times larger than the maximum indentation depth.

Taking into account the length scales involved and the sample microstructure, it is statistically unlikely to hit a region where only the matrix is present over a range of 8 μ, as the random distribution of small islands appears to be equally distributed over the matrix.

Under the conditions mentioned above, we consider the big islands relatively homogenous whereas the matrix is considered inherently heterogeneous as the dispersion of small islands is randomly distributed and their grain size distribution is highly variable. In order to be consistent with the assumed homogeneity of the big islands, we discarded the indents that landed on the island's edges or in their close proximity.

Under the assumption of homogeneity of the big islands, it is surprising to record such a large standard deviation for big islands values on each sample. We were expecting large data scattering in the matrix due to the random distribution of the small islands, each distribution contributing differently to the mechanical response. However, large dispersion of the big islands' values requires a different interpretation. Similar dispersions were reported by other studies [61], [62], with different explanations.

A possible explanation to the large scattering for E and H_{IT} on the big islands, despite their assumed homogeneity, could be that the activation reaction taking place in the matrix also affects the mechanical properties of the large unreacted slags. A reaction gradient might exist over the exposed cross section of a big island resulting in a mechanical properties gradient. We remind that on average, only 1 or 2 indentation points are landing on each big island. The large dispersion could also be an effect of the number of big islands indentation points falling below the threshold for statistical significance, although such a threshold is not easily identified. The number of indents landed on the big islands is much smaller compared to the ones landed on the matrix (between 1/2 and 1/3).

Another explanation for the large scattering is that the maximum indentation load, hence the corresponding maximum indentation depths, is not adapted to the sample microstructure. Perhaps a better compromise could be found. Shallower indentations could be tested, allowing the probing of more homogenous volumes while staying sufficiently away from depth regions where surface roughness, area function and indentation size effect do not affect the results. However, shallower indentation would leave smaller residual indents, more difficult to localize by SEM observation, thus further limiting an image-guided approach.

An explanation for the radiation-induced strength increase could be the development of carbonates, such as $CaCO_3$ or Na_2CO_3, within the pores and microcracks [63], [64], as well as the oxidation of Fe. The strength enhancement of iron-rich AAMs can be attributed to the radiolytic effect on the various oxidation states of iron, which is also responsible for the strength of non-irradiated AAMs [65], [66].

The structure and characteristics of AAMs can be considerably altered by high-dose irradiation, according to recent findings. Research has shown that the AAM matrix expands gradually as the irradiation dose rises, which causes microcracks to form and the structural integrity to be

compromised overall [6]. This expansion is most likely the consequence of the major binder in AAMs, aluminosilicate gel, radiolytically breaking down. This process can release trapped gasses and create new molecular species within the matrix [67].

5. Conclusions

The leaching behaviour of structural elements Fe, Na and Al as well as doping elements Cs, Sr, Eu and Ce in samples made with three different slag compositions was investigated, as well as the impact on their leachability after gamma irradiation.

The findings of this work suggest complex variations in the leaching behaviour of different elements across the samples. The highest release in all samples was exhibited by Na. Similarly, to Na, Cs is the second most released element in this study. This can be attributed to the high solubility in water of most of its compounds relevant to this work. Slag S1 formed an iron rich ferrosilicate network, while slags S2 and S3 based on the lower silica content resulted in formation of a calcium-iron silicate network. The presence of Al in slag S1 created greater demand for interstitial cations in the matrix, which led to reduced release of both Na and Cs and contributed to the overall stability of the AAM structure. The release of aluminium was comparable in samples made with slag S1.

The addition of CeO_2 nanoparticles altered the release patterns of some elements. Samples containing CeO_2 nanoparticles exhibited different release trends compared to those without, indicating that the nanoparticles may influence the interactions between elements within the sample matrix, affecting their leaching behaviour. The presence of cerium in samples made with slag S3 lowered the release of iron. Europium releases were lower for samples doped with CeO_2 nanoparticles for slags S1 and S2. For samples with slag S3 it was not the case.

Furthermore, the leaching study in this work reveals that gamma irradiation affects the mobility and stability of several elements in Fe-rich AAMs. The mobility of Na and Eu is specifically increased after irradiation, whereas Fe, Al, Cs, and Sr are better retained inside the matrix. Gamma irradiation results in radiolysis, which ionizes water and causes the leachates to become more acidic, lowering their pH levels. In early eluates of irradiated samples, Cs release decreases while Na release rises. The gamma irradiation causes Fe to oxidize from Fe^{2+} to Fe^{3+}, which leads to its incorporation into the matrix and consequently lower leaching levels after irradiation. More research is needed to fully understand Fe-rich slag-based AAMs' ability to immobilize higher oxidation state metals, although they show promise for immobilizing radioactive waste, particularly for elements like Cs and Sr. Strontium release was steadily low for all cases. Overall, the leaching of the dopants Sr, Eu and Ce was minimal, proving the effectiveness of the immobilisation abilities of the AAMs studied in this work.

In terms of mechanical properties, nanoindentation results are complicated by the material's heterogeneity. The distribution of different phases makes accurate measurement challenging, as variations in phase distribution led to scattered data. Shallower indentations may help isolate the matrix properties, but surface roughness and size effects must be considered. Furthermore, irradiation can potentially strengthen Fe-rich AAM matrices by forming carbonates or by oxidizing Fe. Higher radiation dosages, however, may also result in matrix expansion, which could induce microcracking and structural deterioration. Increasing the number of indentation points (larger grids with less spacing) could improve the statistics for the big islands, but the time-consuming indexing work in our image-guided approach excludes its application to large grids.

Understanding the precise role of CeO_2 nanoparticles in modifying the leaching behaviour is crucial. For instance, investigating whether these nanoparticles act as nucleation sites, alter the pore structure, or participate in chemical reactions within the AAM matrix can provide valuable insights. Additionally, exploring the potential synergistic effects between CeO_2 nanoparticles and other elements (such as Sr, Eu, and Fe) could lead to the development of AAMs with tailored properties for specific applications. Furthermore, assessing the environmental impact and practical implications of using iron-rich AAM structures with CeO_2 nanoparticles in real-world applications is essential. Future work could include developing alkali-activated compositions that are more resistant to radiolytic degradation in order to mitigate the impact of high-dose irradiation. Additionally, the use of advanced imaging techniques, such as the ones employed in this study, can provide valuable insights into the mechanisms causing the radiation-induced degradation of alkali-activated materials. This information could ultimately contribute to the development of more resilient and reliable alkali-activated-based materials for their use in the immobilisation of radionuclides.

Acknowledgements

The authors would like to thank Rudy Konings, Karin Popa, Markus Ernstberger, Antonio Bulgheroni, Patrick Lajarge for their support, Tobias Hertel and Yiannis Pontikes (SREMat) for their help in the production of the slag, Britta Bergfeldt for conducting the XRF measurements in the lab for bulk analysis at the Institute for Technical Chemistry KIT. This work was realized with the collaboration of the European Commission Joint Research Centre under the Collaborative Doctoral Partnership Agreement No 35342.

References

[1] R. Burcl, “Radioactive waste (RAW) categories, characterization and processing route selection,” in *Radioactive Waste Management and Contaminated Site Clean-Up: Processes, Technologies and International Experience*, Elsevier Inc., 2013, pp. 50–72.

[2] Z. Drace and M. I. Ojovan, “The Behaviours of Cementitious Materials in Long Term Storage and Disposal: An Overview of Results of the IAEA Coordinated Research Project,” *MRS Online Proc. Libr.*, vol. 1193, p. 663, 2009.

[3] G. Modolo, A. Wilden, A. Geist, D. Magnusson, and R. Malmbeck, “A review of the demonstration of innovative solvent extraction processes for the recovery of trivalent minor actinides from PUREX raffinate,” *Radiochim. Acta*, vol. 100, no. 8–9, pp. 715–725, 2012, doi: 10.1524/ract.2012.1962.

[4] S. Patra, E. Roy, R. Madhuri, and P. K. Sharma, “Fast and selective preconcentration of europium from wastewater and coal soil by graphene oxide/silane@Fe3O4 dendritic nanostructure,” *Environ. Sci. Technol.*, vol. 49, no. 10, pp. 6117–6126, 2015, doi: 10.1021/acs.est.5b00182.

[5] Y. Sun, Q. Wang, C. Chen, X. Tan, and X. Wang, “Interaction between Eu(III) and graphene oxide nanosheets investigated by batch and extended X-ray absorption fine structure spectroscopy and by modeling techniques,” *Environ. Sci. Technol.*, vol. 46, no. 11, pp. 6020–6027, 2012, doi: 10.1021/es300720f.

[6] Z. G. Ralli and S. J. Pantazopoulou, “State of the art on geopolymer concrete,” *Int. J. Struct. Integr.*, vol. 12, no. 4, pp. 511–533, 2020, doi: 10.1108/IJSI-05-2020-0050.

[7] B. V. Rangan, D. Hardjito, S. E. Wallah, and M. J. Sumajouw, “Studies on Fly Ash-based Geopolymer Concrete,” *Geopolymer green Chem. Sustain. Dev. Solut. Stud.*, pp. 133–137, 2005.

[8] S. E. Wallah and B. V Rangan, “LOW-CALCIUM FLY ASH-BASED By Curtin University of Technology,” 2006.

[9] D. Tavor, A. Wolfson, A. Shamaev, and A. Shvarzman, “Recycling of Industrial Wastewater by Its Immobilization in Geopolymer Cement,” *Ind. Eng. Chem. Res.*, vol. 46, pp. 6801–6805, 2007.

[10] P. Krivenko, “Why alkaline activation - 60 years of the theory and practice of alkali-activated materials,” *J. Ceram. Sci. Technol.*, vol. 8, no. 3, pp. 323–333, 2017, doi: 10.4416/JCST2017-00042.

[11] J. L. Provis and J. S. J. Van Deventer, *Introduction to geopolymers*, no. 1940. Woodhead Publishing Limited, 2009.

[12] B. Walkley, X. Ke, O. H. Hussein, S. A. Bernal, and J. L. Provis, “Incorporation of strontium and calcium in geopolymer gels,” *J. Hazard. Mater.*, vol. 382, no. June 2019, p. 121015, 2020, doi: 10.1016/j.jhazmat.2019.121015.

[13] E. Mukiza, Q. T. Phung, L. Frederickx, D. Jacques, S. Seetharam, and G. De Schutter, “Co-immobilization of cesium and strontium containing waste by metakaolin-based geopolymer: Microstructure, mineralogy and mechanical properties,” *J. Nucl. Mater.*, vol. 585, no. June, p. 154639, 2023, doi: 10.1016/j.jnucmat.2023.154639.

[14] M. Komljenović, G. Tanasijević, N. Džunuzović, and J. L. Provis, “Immobilization of cesium with alkali-activated blast furnace slag,” *J. Hazard. Mater.*, vol. 388, no. October 2019, 2020, doi:

10.1016/j.jhazmat.2019.121765.

[15] J. L. Provis, “Geopolymers and other alkali activated materials: Why, how, and what?,” *Mater. Struct. Constr.*, vol. 47, no. 1–2, pp. 11–25, 2014, doi: 10.1617/s11527-013-0211-5.

[16] F. Fan, Z. Liu, G. Xu, H. Peng, and C. S. Cai, “Mechanical and thermal properties of fly ash based geopolymers,” *Constr. Build. Mater.*, vol. 160, pp. 66–81, 2018, doi: 10.1016/j.conbuildmat.2017.11.023.

[17] N. Deng *et al.*, “Effects of gamma-ray irradiation on leaching of simulated 133Cs+ radionuclides from geopolymer wasteforms,” *J. Nucl. Mater.*, vol. 459, pp. 270–275, 2015, doi: 10.1016/j.jnucmat.2015.01.052.

[18] Z. Xu *et al.*, “Immobilization of strontium-loaded zeolite A by metakaolin based-geopolymer,” *Ceram. Int.*, vol. 43, no. 5, pp. 4434–4439, 2017, doi: 10.1016/j.ceramint.2016.12.092.

[19] K. Shiota, T. Nakamura, M. Takaoka, S. F. Aminuddin, K. Oshita, and T. Fujimori, “Stabilization of cesium in alkali-activated municipal solid waste incineration fly ash and a pyrophyllite-based system,” *Chemosphere*, vol. 187, no. March 2011, pp. 188–195, 2017, doi: 10.1016/j.chemosphere.2017.08.114.

[20] J. Y. Goo, B. J. Kim, M. Kang, J. Jeong, H. Y. Jo, and J. S. Kwon, “Leaching behavior of cesium, strontium, cobalt, and europium from immobilized cement matrix,” *Appl. Sci.*, vol. 11, no. 18, 2021, doi: 10.3390/app11188418.

[21] N. Vandevenne *et al.*, “Alkali-activated materials for radionuclide immobilisation and the effect of precursor composition on Cs/Sr retention,” *J. Nucl. Mater.*, vol. 510, pp. 575–584, 2018, doi: 10.1016/j.jnucmat.2018.08.045.

[22] J. Zhang, J. L. Provis, D. Feng, and J. S. J. van Deventer, “Geopolymers for immobilization of Cr6+, Cd2+, and Pb2+,” *J. Hazard. Mater.*, vol. 157, no. 2–3, pp. 587–598, Sep. 2008, doi: 10.1016/j.jhazmat.2008.01.053.

[23] T. Hanzlicek, M. Steinerova, and P. Straka, “Radioactive metal isotopes stabilized in a geopolymer matrix: Determination of a leaching extract by a radiotracer method,” *J. Am. Ceram. Soc.*, vol. 89, no. 11, pp. 3541–3543, 2006, doi: 10.1111/j.1551-2916.2006.01024.x.

[24] P. Lichvar, M. Rozloznik, and S. Sekely, “Behaviour of Aluminosilicate Inorganic Matrix SIAL During and After Solidification of Radioactive Sludge and Radioactive Spent Resins and Their Mixtures,” *Amec Nucl. Slovakia*, vol. 137, pp. 1–16, 2013.

[25] M. R. El-Naggar, “Applicability of alkali activated slag-seeded Egyptian Sinai kaolin for the immobilization of 60Co radionuclide,” *J. Nucl. Mater.*, vol. 447, no. 1–3, pp. 15–21, 2014, doi: 10.1016/j.jnucmat.2013.12.020.

[26] C. C. Pavel, M. Walter, P. Pöml, D. Bouëxière, and K. Popa, “Contrasting immobilization behavior of Cs+ and Sr2+ cations in a titanosilicate matrix,” *J. Mater. Chem.*, vol. 21, no. 11, pp. 3831–3837, 2011, doi: 10.1039/c0jm03135f.

[27] K. Popa and C. C. Pavel, “Radioactive wastewaters purification using titanosilicates materials: State of the art and perspectives,” *Desalination*, vol. 293, pp. 78–86, 2012, doi: 10.1016/j.desal.2012.02.027.

[28] N. Vandevenne *et al.*, “Incorporating Cs and Sr into blast furnace slag inorganic polymers and their effect on matrix properties,” *J. Nucl. Mater.*, vol. 503, pp. 1–12, 2018, doi: 10.1016/j.jnucmat.2018.02.023.

[29] D. Comandella *et al.*, “Recovery of rare earth elements by nanometric CeO2embedded into

electrospun PVA nanofibres," *RSC Adv.*, vol. 11, no. 32, pp. 19351–19362, 2021, doi: 10.1039/d1ra02097h.

[30] K. Gijbels, R. Ion Iacobescu, Y. Pontikes, N. Vandevenne, S. Schreurs, and W. Schroeyers, "Radon immobilization potential of alkali-activated materials containing ground granulated blast furnace slag and phosphogypsum," *Constr. Build. Mater.*, vol. 184, pp. 68–75, 2018, doi: 10.1016/j.conbuildmat.2018.06.162.

[31] N. M. Piatak, M. B. Parsons, and R. R. Seal, *Characteristics and environmental aspects of slag : A review*, vol. 57. Elsevier Ltd, 2015.

[32] S. Onisei, A. P. Douvalis, A. Malfliet, A. Peys, and Y. Pontikes, "Inorganic polymers made of fayalite slag: On the microstructure and behavior of Fe," *J. Am. Ceram. Soc.*, vol. 101, no. 6, pp. 2245–2257, 2018, doi: 10.1111/jace.15420.

[33] G. Martínez-Barrera *et al.*, "Gamma Radiation as a Recycling Tool for Waste Materials Used in Concrete," *Evol. Ioniz. Radiat. Res.*, 2015, doi: 10.5772/60435.

[34] B. Mast *et al.*, "The effect of high dose rate gamma irradiation on the curing of CaO-FexOy-SiO2 slag based inorganic polymers: Mechanical and microstructural analysis," *J. Nucl. Mater.*, vol. 539, p. 152237, 2020, doi: 10.1016/j.jnucmat.2020.152237.

[35] K. Wiszumirska *et al.*, "Characterization of Biodegradable Food Contact Materials under Gamma-Radiation Treatment," *Materials (Basel).*, vol. 16, no. 2, 2023, doi: 10.3390/ma16020859.

[36] M. L. Y. Yeoh *et al.*, "Mechanistic impacts of long-term gamma irradiation on physicochemical, structural, and mechanical stabilities of radiation-responsive geopolymer pastes," *J. Hazard. Mater.*, vol. 407, no. November 2020, p. 124805, 2021, doi: 10.1016/j.jhazmat.2020.124805.

[37] M. A. Mahrous *et al.*, "Investigating irradiation effects on metakaolin-based geopolymer Investigating irradiation effects on metakaolin-based geopolymer," *Constr. Build. Mater.*, vol. 437, no. June, p. 136837, 2024, doi: 10.1016/j.conbuildmat.2024.136837.

[38] H. A. Van der Sloot, J. C. L. Meeussen, A. C. Garrabrants, D. . S. Kosson, and M. Fuhrmann, "Review of the physical and chemical aspects of leaching assessment," *CBP-TR-2009-002, Rev. 0*, no. November, pp. 1–98, 2009.

[39] H. A. Van der Sloot and D. S. Kosson, "Use of characterisation leaching tests and associated modelling tools in assessing the hazardous nature of wastes," *J. Hazard. Mater.*, vol. 207–208, pp. 36–43, 2012, doi: 10.1016/j.jhazmat.2011.03.119.

[40] P. Zuloaga, C. Andrade Perdrix, and M. Castellote, "Leaching reinforced concrete vaults subjected to variable water content due to capillary suction created by seasonal temperature changes," *RILEM Work. Long-Term Perform. Cem. Barriers Reinf. Concr. Nucl. Power Plants 1-10*, 2009, [Online]. Available: https://digital.csic.es/handle/10261/234015.

[41] European Committee for Standardization, "CEN/TS 16637-3, Construction products: Assessment of release of dangerous substances - Part 3: Horizontal up-flow percolation test," 2016.

[42] Y. Pontikes *et al.*, "Slags with a high Al and Fe content as precursors for inorganic polymers," *Appl. Clay Sci.*, vol. 73, no. 1, pp. 93–102, 2013, doi: 10.1016/j.clay.2012.09.020.

[43] D. Prieur *et al.*, "Size Dependence of Lattice Parameter and Electronic Structure in CeO2 Nanoparticles," *Inorg. Chem.*, vol. 59, no. 8, pp. 5760–5767, 2020, doi:

10.1021/acs.inorgchem.0c00506.

[44] A. Sehgal, Y. Lalatonne, J. Berret, and M. Morvan, “Precipitation-Redispersion of Cerium Oxide Nanoparticles with Poly (Acrylic Acid) : Towards Stable Dispersions II - Experimental III - The precipitation-redispersion phenomenon,” *Langmuir*, vol. 21, no. 20, pp. 9359–9364, 2005.

[45] Z. Černý, T. Černoušek, P. Vácha, K. Sihelská, and V. Tyrpekl, “Development of geopolymer based sacrificial materials for GEN IV severe accident mitigation,” *J. Nucl. Mater.*, vol. 553, 2021, doi: 10.1016/j.jnucmat.2021.153024.

[46] W. C. Oliver and G. M. Pharr, “Measurement of hardness and elastic modulus by instrumented indentation: Advances in understanding and refinements to methodology,” *J. Mater. Res.*, vol. 19, no. 1, pp. 3–20, 2004, doi: 10.1557/jmr.2004.19.1.3.

[47] Z. Ji and Y. Pei, “Bibliographic and visualized analysis of geopolymer research and its application in heavy metal immobilization: A review,” *J. Environ. Manage.*, vol. 231, no. November 2018, pp. 256–267, 2019, doi: 10.1016/j.jenvman.2018.10.041.

[48] J. L. Provis and C. A. Rees, “Geopolymer synthesis kinetics,” *Geopolymers Struct. Process. Prop. Ind. Appl.*, pp. 118–136, 2009, doi: 10.1533/9781845696382.1.118.

[49] D. Lambertin, C. Boher, A. Dannoux-papin, K. Galliez, A. Rooses, and F. Frizon, “Influence of gamma ray irradiation on metakaolin based sodium geopolymer,” *J. Nucl. Mater.*, vol. 443, no. 1–3, pp. 311–315, 2020, doi: 10.1016/j.jnucmat.2013.06.044.

[50] D. Féron, “Overview of nuclear materials and nuclear corrosion science and engineering 2,” *Nucl. Corros. Sci. Eng.*, pp. 31–56, 2012, doi: 10.1533/9780857095343.1.31.

[51] P. Bouniol and A. Aspart, “DISAPPEARANCE OF OXYGEN IN CONCRETE UNDER IRRADIATION: THE ROLE OF PEROXIDES IN RADIOLYSIS,” *Cem. Concr. Res.*, vol. 28, no. 11, pp. 1669–1681, 1998.

[52] T. Jurkin, M. Goti, Š. Goran, and I. Puci, “Gamma-irradiation synthesis of iron oxide nanoparticles in the presence of PEO , PVP or CTAB,” vol. 124, pp. 75–83, 2016, doi: 10.1016/j.radphyschem.2015.11.019.

[53] T. I. Sutherland *et al.*, “Effect of ferrous ion concentration on the kinetics of radiation-induced iron-oxide nanoparticle formation and growth,” *Phys. Chem. Chem. Phys.*, no. 19, pp. 695–708, 2017, doi: 10.1039/c6cp05456k.

[54] S. Simon, G. J. G. Gluth, A. Peys, S. Onisei, D. Banerjee, and Y. Pontikes, “The fate of iron during the alkali-activation of synthetic (CaO-) FeOx-SiO2 slags: An Fe K-edge XANES study,” *J. Am. Ceram. Soc.*, vol. 101, pp. 2107–2118. wileyonlinelibrary.com/journal/jace, 2018, doi: https://doi.org/10.1111/jace.15354.

[55] Peys, C. E. White, H. Rahier, B. Blanpain, and Y. Pontikes, “Alkali-activation of CaO-FeOx-SiO2 slag: Formation mechanism from in-situ X-ray total scattering,” *Cem. Concr. Res.*, vol. 122, no. November 2018, pp. 179–188, 2019, doi: 10.1016/j.cemconres.2019.04.019.

[56] I. Salas, E. Cifrian, L. Soriano, J. Monzó, and A. Andrés, “Environmental assessment of alkali-activated materials based on agro-industrial waste as alkaline activators through leaching tests,” *J. Environ. Manage.*, vol. 368, no. August, 2024, doi: 10.1016/j.jenvman.2024.122265.

[57] M. Giels, R. I. Iacobescu, V. Cappuyns, Y. Pontikes, and J. Elsen, “Understanding the leaching behavior of inorganic polymers made of iron rich slags,” *J. Clean. Prod.*, vol. 238, 2019, doi: 10.1016/j.jclepro.2019.117736.

[58] E. R. Vance and D. S. Perera, “Geopolymers for nuclear waste immobilisation,” *Geopolymers Struct. Process. Prop. Ind. Appl.*, pp. 401–420, 2009, doi: 10.1533/9781845696382.3.401.

[59] G. Constantinides, K. S. Ravi Chandran, F. J. Ulm, and K. J. Van Vliet, “Grid indentation analysis of composite microstructure and mechanics: Principles and validation,” *Mater. Sci. Eng. A*, vol. 430, no. 1–2, pp. 189–202, 2006, doi: 10.1016/j.msea.2006.05.125.

[60] H. Buckle, *The science of hardness testing and its research applications*. 1973.

[61] C. Hu and Z. Li, “A review on the mechanical properties of cement-based materials measured by nanoindentation,” *Constr. Build. Mater.*, vol. 90, pp. 80–90, 2015, doi: 10.1016/j.conbuildmat.2015.05.008.

[62] B. Hilloulin, M. Robira, and A. Loukili, “Coupling statistical indentation and microscopy to evaluate micromechanical properties of materials: Application to viscoelastic behavior of irradiated mortars,” *Cem. Concr. Compos.*, vol. 94, no. February, pp. 153–165, 2018, doi: 10.1016/j.cemconcomp.2018.09.008.

[63] I. Maruyama *et al.*, “Impact of gamma-ray irradiation on hardened white Portland cement pastes exposed to atmosphere,” *Cem. Concr. Res.*, vol. 108, no. June 2017, pp. 59–71, 2018, doi: 10.1016/j.cemconres.2018.03.005.

[64] A. Keulen, A. van Zomeren, and J. J. Dijkstra, “Leaching of monolithic and granular alkali activated slag-fly ash materials, as a function of the mixture design,” *Waste Manag.*, vol. 78, pp. 497–508, 2018, doi: 10.1016/j.wasman.2018.06.019.

[65] Peys, A. P. Douvalis, V. Hallet, H. Rahier, B. Blanpain, and Y. Pontikes, “Inorganic Polymers From CaO-FeOx-SiO2 Slag: The Start of Oxidation of Fe and the Formation of a Mixed Valence Binder,” *Front. Mater.*, vol. 6, no. August, pp. 1–10, 2019, doi: 10.3389/fmats.2019.00212.

[66] A. Peys, C. E. White, D. Olds, H. Rahier, B. Blanpain, and Y. Pontikes, *Molecular structure of CaO–FeOx–SiO2 glassy slags and resultant inorganic polymer binders*, vol. 101, no. 12. 2018.

[67] C. Fang, J. Xie, B. Zhang, B. Yuan, and C. Wang, “Impact properties of geopolymeric concrete: A state-of-the-art review,” *IOP Conf. Ser. Mater. Sci. Eng.*, vol. 284, no. 1, 2018, doi: 10.1088/1757-899X/284/1/012012.